ROYAL SOCIETY
OF CHEMISTRY

PAPER

Check for updates

Grazing incidence X-Ray diffraction: identifying the dominant facet in copper foams that electrocatalyze the reduction of carbon dioxide to formate†

Steven T. Ahn,[a] Sujat Sen [b,c] and G. Tayhas R. Palmore ⋆[a,b]

Copper foams have been shown to electrocatalyze the carbon dioxide reduction reaction (CO_2RR) to formate ($HCOO^-$) with significant faradaic efficiency (FE) at low overpotentials. Unlike the CO_2RR electrocatalyzed at copper foils, the CO_2RR electrocatalyzed at porous copper foams selects for $HCOO^-$ essentially to the exclusion of hydrocarbon products. Formate is an environmentally friendly organic acid with many applications such as food preservation, textile processing, de-icing, and fuel in fuel cells. Thus, $HCOO^-$ is an attractive product from the CO_2RR if it is produced at an overpotential lower than that at other electrocatalysts. In this study, grazing incidence X-ray diffraction (GIXRD) was used to identify the dominant surface facet of porous copper foams that accounts for its selectivity for $HCOO^-$ during the CO_2RR. Included are data from the CO_2RR at different temperatures using copper foams as the electrocatalyst. Under optimal reaction conditions at 2 °C, the FE for converting CO_2 to $HCOO^-$ at Cu foams approaches 50% while the FE for hydrogen gas (H_2) falls below 40%, a significant departure from that obtained at polycrystalline Cu foils. Computational studies by others have proposed (200) and (111) facets of Cu foils thermodynamically favour methane and other hydrocarbons, CO, $HCOO^-$ from the CO_2RR. Results from the GIXRD studies indicate Cu foams are dominated by the (111) facet, which accounts for the selectivity of Cu foams toward $HCOO^-$ regardless of temperature used for the CO_2RR.

Introduction

Electrochemical conversion of CO_2 into higher value products such as liquid fuels (*e.g.*, formic acid) or chemical intermediates (*e.g.*, CO, CH_2CH_2)[1,2] for integration with downstream chemical reactions is an attractive approach to CO_2 utilization in carbon capture, utilization, and storage (CCUS).[3–5] Formic acid (HCOOH) is an appealing target because of its many applications including its use in direct formic acid fuel cells (DFAFCs).[6,7] Sustainable production of HCOOH is a key obstacle to the development of DFAFCs. DFAFC technology coupled with direct air-capture and electrochemical conversion of CO_2 to $HCOO^-$ has the potential to establish a carbon

neutral cycle where renewable energy is stored *via* the CO_2RR and released *via* reverse reaction.[8]

Hori *et al.* screened the CO_2RR at several planar polycrystalline metals at 18.5(5) °C.[9] Copper (Cu) was found to produce hydrocarbons such as ethylene (C_2H_4) and methane (CH_4) while all other metals produced almost exclusively HCOOH and CO along with H_2 from the reduction of water – all two-electron reduction products. Azuma *et al.* compared product selectivity of CO_2RR on several metals at two temperatures: 0 °C and 20 °C.[10] Faradaic efficiencies for formate ($HCOO^-$) generally increased with lower temperature regardless of product selectivity observed at room temperature (RT). Polycrystalline Cu however, exhibited a shift in FE from C_2H_4 and $HCOO^-$ to CH_4 and CO at lower temperatures. Hori *et al.* also observed a similar shift in product selectivity[11] and this shift was confirmed in a recent study.[12]

One of the earliest mechanistic studies on the electroreduction of CO_2 at Cu confirmed that the HCOO* intermediate is favored on the Cu (111) facet.[13] Further supporting these conclusions is the more recent study in which the authors concluded that on Cu(111) "the Eley–Rideal reaction *via* proton-electron transfer may be more favorable during initial CO_2 electroreduction into CO through intermediate COOH,

[a]School of Engineering, Brown University, 184 Hope Street, Providence, RI 02912, USA. E-mail: tayhas_palmore@brown.edu
[b]Department of Chemistry, Brown University, 324 Brook Street, Providence, RI 02912, USA
[c]Department of Chemistry & Biochemistry, University of Wisconsin La Crosse, 1725 State Street, La Crosse, WI 54601, USA

whereas chemisorbed CO_2 reacting with a surface-adsorbed H into $HCOO^-$ *via* Langmuir–Hinshelwood mechanical *is more facile to occur*".[14] Importantly, $HCOO^-$ is kinetically favored (lower transition state energies) over CO formation.

Nanostructured metals often exhibit unique electrocatalytic properties compared to their corresponding bulk form.[15] We have reported studies on the CO_2RR at both nanostructured Cu foams[16] and nanostructured foils Cu.[17] Compared to Cu foils, the selectivity for $HCOO^-$ was enhanced at Cu foams while the FE for CO, CH_4, and C_2H_4 was suppressed. We proposed the CO_2RR at Cu foams followed a mechanistic pathway that proceeded through an adsorbed formate (HCOO*) while the mechanistic pathway through an adsorbed carboxyl (*COOH) and subsequent adsorbed CO (*CO) was suppressed.

In this study, grazing incidence X-ray diffraction (GIXRD) is shown to be a valuable method for identifying the dominant facet present in three-dimensional porous structure such as a Cu foam. By identifying the dominant facet in these porous electrocatalysts, we can confirm that $HCOO^-$ is produced at Cu foams *via* an adsorbed formate (HCOO*) pathway to the exclusion of C_{1+} products such as CH_4 and C_2H_4 even at different temperatures. We show that GIXRD is a reliable method for probing surface faceting of as-prepared electrodes that eliminates signal from any underlying substrate such as polycrystalline Cu, Cu cubes[18] or current collector (*e.g.*, carbon-supported Cu nanoparticles).[19]

Experimental

Chemicals and equipment

Copper sulfate pentahydrate ($CuSO_4 \cdot 5H_2O$, 99.98%, Fisher Scientific), sulfuric acid (H_2SO_4, 98%, Fisher Scientific), potassium bicarbonate ($KHCO_3$, ≥99.95%, Sigma Aldrich), carbon dioxide (CO_2, 99.995% laser grade, Praxair), and nitrogen gas (N_2, 99.999%, Corp Brothers) were used as received. Electrodes were fabricated from copper foil (0.25 mm thickness, 99.9%, Goodfellow). Deionized water (18.2 MΩ, Milli-Q water purification system) was used for all solutions and pH was measured using a Fisher Scientific Accumet Basic AB15 pH meter equipped with a pH/ATC electrode. Contact angle was measured on a Ramé-hart 100-25-M goniometer. 1D ^{1}H nuclear magnetic resonance (NMR) spectra were recorded on a Bruker Avance DRX400 (400 MHz) spectrometer. Gaseous products were analysed using a Buck Scientific 910 gas chromatograph (GC) in the Multiple Gas #3 configuration with automated sample loop. Copper foam electrodes were prepared as previously described[16,20] using an electrodeposition time of 10 seconds unless otherwise indicated.

Structural characterization

Copper foam electrodes were characterized by X-ray diffraction (XRD), scanning electron microscopy (SEM), and transmission electron microscopy (TEM). Powder and grazing incidence XRD (GIXRD) were performed on a Bruker D8 Discover diffractometer using monochromatic Cu-Kα radiation at 40 kV and 40 mA. Powder XRD experiments utilized a LYNXEYE detector

and were performed at 2θ steps of 0.01° and acquisition time of 0.40 s per step. GIXRD experiments utilized a scintillation counter and were performed at 2θ steps of 0.01° and acquisition time of 0.80 s per step. A LEO 1530 scanning electron microscope (SEM) coupled with energy-dispersive spectroscopy (EDS) was used to determine stoichiometry of the Cu foams. High-resolution TEM (HRTEM) and selected area electron diffraction (SAED) were performed on a JEOL 2100F transmission electron microscope also coupled with EDS.

Electrochemical experiments

Electrochemical impedance spectroscopy (EIS), cyclic voltammetry (CV), and controlled potential electrolysis experiments were performed on a Princeton Applied Research VersaSTAT4-500 potentiostat. A Nafion 117 proton-exchange membrane separated the two compartments of a gas-tight H-cell. The three-electrode configuration included a working electrode of copper foam electrodeposited onto a copper substrate, a counter electrode of platinum gauze (99.9%, Alfa Aesar), and a leak-proof Ag/AgCl reference electrode (+197 mV *vs.* SHE). All potentials are reported *vs.* Ag/AgCl unless otherwise indicated. Catholyte and anolyte volumes were 8 mL each and the headspace volume was *ca.* 24 mL (note: minimizing headspace volume was not necessary as the cell was connected directly to the sample loop of the GC and adequately degassed (*vide infra*)). The electrolyte solution was 0.1 M $KHCO_3/H_2O$, which was saturated with CO_2 at a flow rate of 30 mL min^{-1} for a minimum of 30 min prior to any experiments or measurements. The absence of ambient air was confirmed prior to any electrochemical experiments by monitoring the O_2 peak in the thermal conductivity detector (TCD) channel of the GC (*vide infra*).

Product analysis

Liquid products were analysed by 1D ^{1}H NMR spectroscopy to circumvent the need to remove electrolyte salts ($KHCO_3$). Each 0.50 mL sample of catholyte was mixed with 25 µL of a D_2O solution containing 10 mM dimethyl sulfoxide (DMSO) and 50 mM phenol used as internal standards. A modified version of the WET procedure (Bruker) allowed for suppression of the H_2O solvent peak at *ca.* δ 4.70.[21] The WET procedure (modified or unmodified) is particularly useful for measuring NMR spectra of samples in mixtures of D_2O and H_2O. The same acquisition parameters were chosen for all NMR spectra, notably 64 scans for a clearer distinction between resonance peaks and baseline noise.

Gaseous products were analysed on a GC equipped with both a flame ionization detector (FID) and a thermal conductivity detector (TCD). The headspace of the electrochemical cell was connected to the GC sample loop, using CO_2 as the eluent stream carrier at 30 ccm. Before arrival at the detectors, hydrogen (H_2), carbon monoxide (CO), and methane (CH_4) were separated by a Molecular Sieve 13x column, and all other C1–C6 compounds were separated by a Hayesep-D column. Hydrogen was quantified on the TCD, while all the other species (CO, CH_4, C_2H_4 *etc.*) were passed through a methanizer before quantification *via* the FID. A bubbler was then connected to the back end of the loop to guarantee a gas-tight system. Gaseous

products were analysed after at least 60 min from the start of CO_2 saturation to ensure adequate degassing of connections and at least three times at random time points during electrolysis.

Temperature control

The temperature of the electrolytic cell was controlled using a circulating water bath (VWR 1160) taking care to prevent contamination of the electrochemical cell. A jacketed beaker filled with deionized H_2O was connected to the circulating water bath. The electrolytic cell was sealed prior to immersion into the water-filled beaker. The temperature inside the cell was confirmed against the temperature setting of the water bath using an ISO 17025 calibrated probe thermometer (accuracy ±0.1 °C, Robo Traceable, Fisher Scientific). This confirmation was done prior to any experiments or measurements and after at least 30 min of saturation with CO_2.

pH measurements

The pH of a solution is temperature dependent. Although the buffering capacity of the electrolyte minimizes any increase in pH, it should be considered when calculating energetic efficiency (EE, see ESI†). A combination pH/ATC electrode was used to measure pH instead of a typical glass pH electrode because the calculation of EE relies on accurate values of pH.

The standard Gibbs free energies of formation (ΔG_f°) of $CO_2(g)$ and $HCOO^-(aq)$ are −394.39 kJ mol^{-1} and −351.00 kJ mol^{-1}, respectively.[22] Using these values, the standard potential of the reaction $CO_2(g) + H^+(aq) + 2e^- \rightarrow HCOO^-(aq)$ is −0.22 V (vs. SHE) at pH 0 and 25 °C (ref. 23) and −0.63 V (vs. SHE) at pH 6.8 and 25 °C. Potentials reported in this study are referenced to the Ag/AgCl electrode (+197 mV vs. SHE), therefore standard potentials and EE were calculated as follows:

$$E_{Ag/AgCl} = E^\circ - 1.98 \times 10^{-4} \cdot T \cdot pH - 0.197 \quad (1)$$

$$EE = \frac{E_{Ag/AgCl} \cdot FE}{E(V\,vs.\,Ag/AgCl)} \quad (2)$$

where E corresponds to the applied electrolysis potential (vs. Ag/AgCl) and pH and temperature are measured values.

iR compensation

Potentiostatic EIS was performed to determine solution resistance (R_s).[24,25] Initially, EIS was measured from 1 MHz to 0.1 Hz at both open circuit voltage and at −1.6 V (vs. Ag/AgCl) to determine a frequency within the ionic and dipolar relaxation regime (ca. 10^4 to 10^7 Hz). For the system studied this value was 10 kHz.[25] Subsequently, the potentiostat was set to compensate for 100% of R_s and was monitored closely for system instability and/or oscillations.[26]

Results and discussion

Industrial-scale CO_2 conversion requires electrocatalysts that are highly selective (i.e., achieve FEs close to 100%), produce products that are self-separating (e.g., $HCOO^-$ in solution phase and H_2 in gaseous phase), and operate at high current densities (ss. high production rates) at low overpotentials. The product distribution and product selectivity for the CO_2RR at dendritic Cu foams (Fig. 1) differ from planar polycrystalline Cu foils notably with FEs shifting away from C_{1+} hydrocarbons such as CH_4 and C_2H_4 at Cu foils towards $HCOO^-$ at Cu foams (Table 1).[16,18,27–29]

The mechanistic pathway for CO_2 electroreduction initiates via adsorbed intermediates HCOO* or *COOH and changes with metal used (e.g., Cu vs. Sn) as well as the specific crystal facet available (e.g., Cu(100) vs. Cu(110) vs. Cu(111) vs. stepped Cu(211)). For example, the Cu(200) facet has been attributed to the increase in $HCOO^-$ production observed at Cu foams.[16] On oxide-derived Cu foams, Cu(200) and Cu(220) peaks are prominent in the post-mortem XRD patterns.[30] The intensity of the Cu(200) peak was reported to be ca. 2.33 times greater (i.e., normalized intensity ratio 0.35/0.15) than that of the Cu(220) peak. Several studies of the CO_2RR on Cu cubes however, have proposed instead that Cu(100) (an equivalent 200 facet) preferentially yields C_2H_4, not $HCOO^-$.[18,31] Electrodes were examined by XRD before and after CO2RR at reducing potentials in aqueous electrolyte. Under these conditions, in situ formation of Cu_xO was not observed (i.e., Fig. S1† is representative of the Cu foams before and after CO2RR).

GIXRD experiments

Conventional θ–2θ (i.e., Bragg–Brentano) geometry for XRD experiments has limited use on thin films of metal foams because it is difficult to differentiate the contribution to peak intensity by the metal foam from the underlying metal substrate. Because the contribution of the underlying Cu substrate to the XRD of Cu foams was not determined previously,[16,30] grazing incidence XRD (GIXRD)[32–34] was used to characterize unequivocally the dominant surface facets of Cu foams (Fig. 2 and Fig. S2†).

Detector counts (i.e., peak intensity) are shown on the left ordinates of Fig. 2a through Fig. 2c to highlight the differences
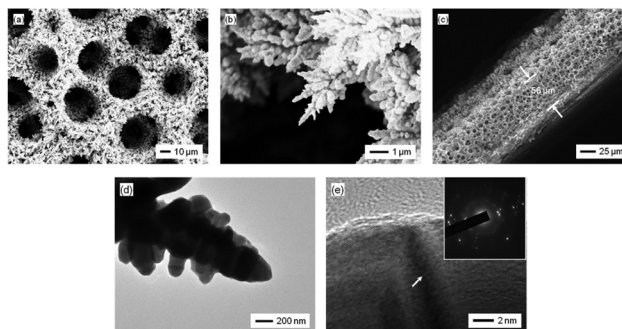

Fig. 1 SEM images of a Cu-foam electrode: (a) porous nature of electrocatalyst, (b) dendritic structures within the pores, (c) cross-sectional view that reveals the thickness of the electrodeposited foam. (d) TEM image of a dendritic structure and (e) HR-TEM image of multiple grains with arrow indicating a grain boundary (SAPD inset).

Table 1 Conditions and results for electroreduction of CO_2 to $HCOO^-$ at Cu- and Cu_2O-based electrocatalysts

Cathode	$HCOO^-$ metrics					T (°C)	N.B.	Ref.
	E (V vs. Ag/AgCl)	FE (%)	EE (%)	$J_{overall}$ (mA cm^{-2})	$J_{partial}$ (mA cm^{-2})			
Cu foam	−1.3	48(2)	29(1)	−2.0	−1.0	2.0 (1)	—	This work
P4VP/Cu	−1.3	40(3)	19(1)	ca. −0.7	ca. −0.3	NR^a	Hybrid system	27
Cu cubes	ca. −1.3	ca. 17	ca. 11	NR	NR	NR^a	Optimized for C_2H_4	18
Cu foam	−1.3 V to −1.5	34(6) to 37 (2)	20(4) to 18.7 (9)	ca. −2.4 to ca. −4.0	ca. −0.8 to ca. −1.5	NR^a	See ESI	16
Cu flower	−1.6	ca. 50	ca. 18	ca. −18	ca. −9.0	10	—	28
Air-annealed Cu	−0.9	33	24.9	ca. −2.7	ca. 0.9	NR^a	FE for CO ca. 40%	29

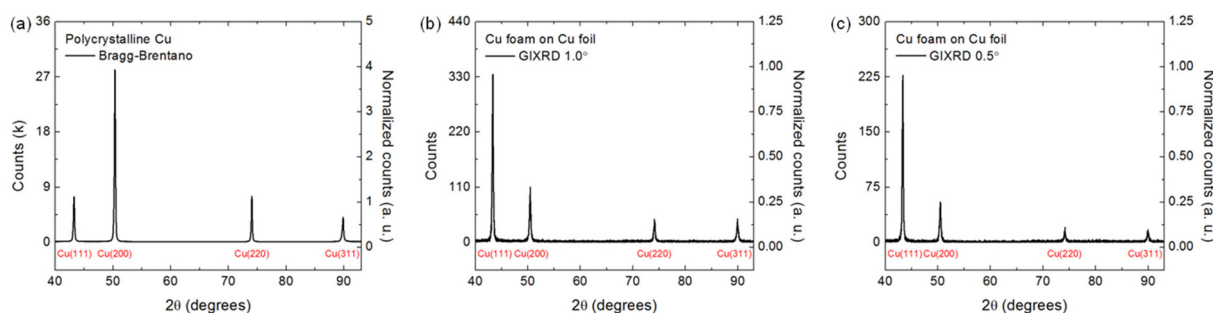^{a} NR = not reported, assumed 22 °C or room temperature (RT).

Fig. 2 (a) θ–2θ (i.e., Bragg−Brentano) XRD pattern of a Cu substrate, (b) and (c) GIXRD patterns of Cu foams electrodeposited onto a Cu substrate, with right ordinates normalized to intensity of the Cu(111) peak. Red labels identify the peaks for polycrystalline Cu (JCPDS 00-004-0836).

between θ–2θ XRD and GIXRD diffractograms. In the GIXRD diffractograms, a small incidence angle (e.g., 1.0° or 0.5°) limits the penetration depth of the X-ray beam and therefore Bragg reflections come only from the surface of the sample, which in this study is the Cu foam excluding the Cu substrate. The intensity of the incoming beam however is increasingly lost at smaller angles with corresponding decrease in detector counts. Most of the incoming beam strikes the stage or bypasses the sample. Detector counts for the GIXRD experiments correspondingly decreased as the incidence angle decreased from 8.0° to 0.5° (Fig. 2 and S2†).‡

The Cu(200) peak at 2θ = 50.3° dominates the θ–2θ XRD of the polycrystalline Cu substrate (Fig. 2a) whereas the Cu(111) peak at 2θ = 43.3° dominates the GIXRD of the Cu foam (Fig. 2b and c). The ratio of Cu(200)/Cu(111) decreases from 3.78 (Fig. 2a) to 0.33 (Fig. 2b). The Cu(111) peak dominates the diffractogram of the Cu foam even more in the 0.5° GIXRD where the ratio of Cu(200)/Cu(111) decreases further to 0.23 (Fig. 2c).

Because the Cu foam and Cu substrate have peaks at identical locations in the XRD, the degree to which peaks from the underlying substrate contribute to the total detector count in the GIXRD is indeterminate. Consequently, molybdenum and platinum were chosen as underlying substrates to Cu foams to aid in the GI-XRD analysis. These two metals are poor catalysts for CO2RR,[35–37] thus insuring that CO2RR only occurs at the Cu foam layer when deposited on Mo or Pt substrates. Cu foams were electrodeposited onto molybdenum (Mo) (Fig. 3 and S3†) and platinum (Pt) (Fig. 4 and S4†) substrates to confirm that peak counts in the GIXRD are due to the Cu foam exclusively. Moreover, Mo and Pt substrates were chosen to rule out the possibility of substrate-influenced epitaxial growth of the Cu foam. Identical GIXRD were obtained regardless of substrate, confirming that Cu foams electrodeposited on different metals including Cu foils with other dominant textures[16,30] is the result of non-epitaxial growth. Results from the GIXRD studies of Cu foams on different substrates demonstrate that GIXRD can distinguish the contribution to the total detector count from Cu foams and an underlying metallic substrate.

The diffractograms (θ–2θ XRD) of Mo and Pt substrates are shown in Fig. 3a and 4a, respectively. Diffractograms of Cu foams electrodeposited onto Mo (Fig. 3b) and Pt substrates
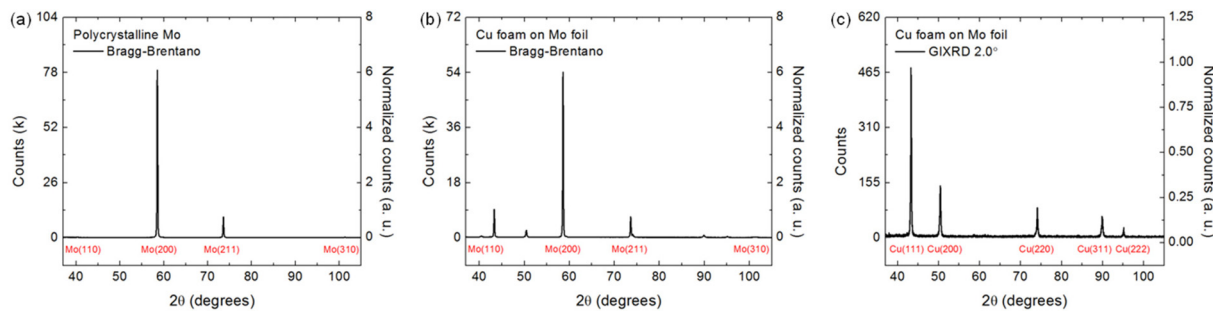
‡Note that the incidence angles chosen herein are larger than angles typically used in GIXRD studies and bridge the oft-neglected intermediate gap between the conventional θ–2θ and typical GIXRD geometries.

Fig. 3 (a) θ–2θ (*i.e.*, Bragg–Brentano) XRD pattern of a Mo substrate, (b) θ–2θ (*i.e.*, Bragg–Brentano) XRD pattern of Cu foams electrodeposited onto a Mo substrate, and (c) GIXRD patterns for θ = 2.0° of Cu foams electrodeposited onto a Mo substrate, with right ordinates normalized to intensity of the Cu(111) peak wherever possible. Red labels identify the peaks for polycrystalline Cu (JCPDS 00-004-0836) and polycrystalline Mo (JCPDS 00-0040809).
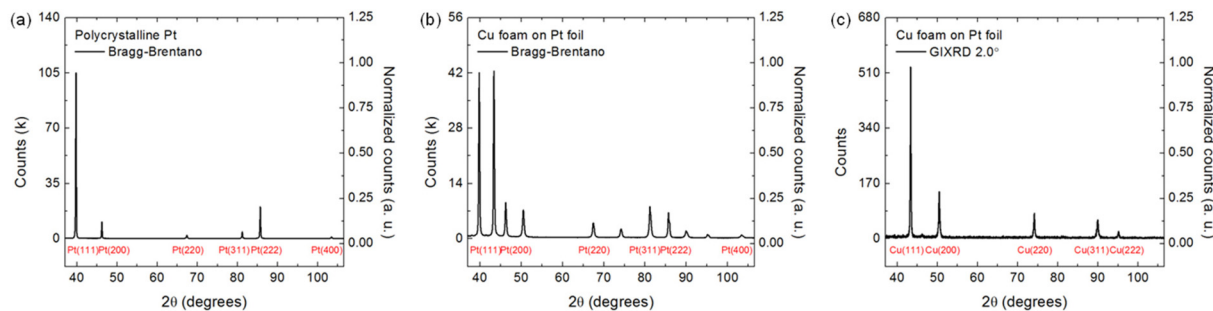

Fig. 4 (a) θ–2θ (*i.e.*, Bragg–Brentano) XRD pattern of a Pt substrate, (b) θ–2θ (*i.e.*, Bragg–Brentano) XRD pattern of Cu foams electrodeposited onto a Pt substrate, and (c) GIXRD patterns for θ = 2.0° of Cu foams electrodeposited onto a Pt substrate, with right ordinates normalized to intensity of the Cu(111) peak wherever possible. Red labels identify the peaks for polycrystalline Cu (JCPDS 00-004-0836) and polycrystalline Pt (JCPDS 00-004-0802).

(Fig. 4b) include the peaks corresponding to the respective underlying substrates, which is expected for such a porous material (Fig. 1). Regardless of substrate used, peaks due to the substrate disappear when the incidence angle is ≤2.0° (Fig. 3c, 4c and Fig. S3, S4†). For comparison, Fig. 2b and c show diffraction patterns of Cu foams deposited on Cu substrates from GIXRD experiments performed at 1.0° or 0.5° respectively, both of which exclude any contribution from the underlying substrate to peak intensity.

Hori *et al.* observed that the FE for HCOO⁻ increased in the transition from a Cu(100) surface to a Cu(111) surface *via* Cu(S)-[n(100) × (111)] in step notation.[38] Moreover, several computational studies indicate that the most positive limiting potential for the formation of HCOO⁻ on Cu electrodes occurs on the Cu(111) facet *via* the HCOO* intermediate.[39,40] Thus, GIXRD data of Cu foams indicates that preferential production of HCOO⁻ at Cu foams is due to a surface dominated by Cu(111), which favours the adsorbed HCOO* intermediate.

Crystallite size and porosity of Cu foams

Even though Cu(111) dominates the surface of Cu foams, the size of Cu(111) and other crystallites is important to consider because of the role of grain boundaries on the CO₂RR.[41]

Particularly relevant for Cu foams is the size of the crystallites relative to the size of the dendrites and whether grain boundaries are expected to affect product distribution and product selectivity of the CO₂RR. Crystallite size was estimated from peak broadening in the 1° and 0.5° GIXRD experiments and the Debye–Scherrer equation:

$$D_{hkl} = \frac{K\lambda}{B_{hkl}\cos\theta} \tag{3}$$

where D_{hkl} is the distance in the hkl direction, K depends on crystallite shape (in this case, K = 0.9), λ is the wavelength of the X-ray beam, B_{hkl} is the peak width at half height, and θ is the Bragg angle. Based on the Cu(111) and Cu(200) peaks in Fig. 2c, the respective diameters were 39.8(9) nm and 28.4(9) nm, both of which are smaller than the size of the dendrites within the pores.

Because the contribution to peak broadening from the instrument is generally higher for the GIXRD *vs.* θ–2θ XRD geometry (*e.g.*, due to a larger beam footprint),[34] GIXRD data has been argued to be unsuitable for use with the Debye–Scherrer equation or Williamson-Hall analysis.[42] Crystallite size was therefore confirmed from peak broadening in the θ–2θ XRD experiments of Cu foams electrodeposited onto Mo and Pt foils. For the Cu(111) peak, the diameter of crystallites on the

Mo substrate was 41.3 nm and on the Pt substrate was 38.2 nm; for the Cu(200) peak, the diameters were respectively 32.6 nm and 23.6 nm. The branch size is on the order of 100 nm (Fig. 1d) and therefore each branch comprises several crystallites (Fig. 1e).

A secondary benefit of using GIXRD to analyse Cu foams is being able to determine the overall porosity of Cu foams *vs.* the hierarchical porosity reported earlier.[16] The attenuated intensity shown in a diffraction pattern can be estimated by the following equation:[32]

$$f = 1 - \exp\left[\frac{\mu \cdot d}{\sin \alpha}\right] \quad (4)$$

where f is the attenuated intensity normalized to the beam intensity, μ is the linear absorption coefficient of the material, d is thickness to be determined, and α is the incidence angle in radians. Based on an approximation that the contribution of the metallic substrate to a GIXRD spectrum disappears when attenuated intensity becomes $1/e$ of the beam intensity (*i.e.*, $f = 1/e$)[33] and using both an incidence angle of $2.0°$ and linear absorption coefficient for Cu of 42 cm^{-1} (at 40 keV) (*vide supra*),[43,44] the thickness of a Cu foam is *ca.* 8.3 μm (based on a dense non-porous thin film). Because the Cu foams possess hierarchical porosity where most of the volume is void space, the actual thickness is *ca.* 56 μm (see Fig. 1c). The estimated porosity therefore is *ca.* 85% (*i.e.*, (56 μm–8.3 μm)/56 μm), which is consistent with a packing efficiency of 91% for close-packed pores in 2-dimensional space.

CO$_2$RR at Cu foams *vs.* temperature and applied potential

Clathrate hydrates are a promising medium for CO$_2$ capture at lower temperatures[45] while amines are commonly used for CO$_2$ capture at ambient temperatures. While an industrial process for CCUS technologies might first release CO$_2$ *via* temperature and/or pressure swing to ambient conditions before electroreduction, examining the effect of electrolyte temperature on product distribution and product selectivity can inform optimal operating conditions for such a process. Therefore, the CO$_2$RR was performed at Cu foams at temperatures ranging from 2 °C (near maximum temperatures for maintaining clathrate hydrates)[46] to 42 °C (near minimum temperatures studied for CO$_2$ capture *via* monoethanolamine).[47,48] In addition, because the limiting potential for the HER on Cu(111) (−0.20 V *vs.* RHE) is slightly more negative than the equilibrium potential for the electroreduction of CO$_2$ to HCOO$^-$ (−0.17 V *vs.* RHE),[39] a working potential of −1.30 V *vs.* Ag/AgCl (−0.71 V *vs.* RHE) was used to optimize formic acid production relative to the HER (Fig. 5). Moreover, the current density (*ss.* reaction rate) at this potential was more than two-fold higher than that at −1.2 V at 22.0 (1) °C (Fig. S5d†).

The FE and EE for HCOO$^-$ increased with decreasing temperature (Fig. 5a and b) and FE shifted away from H$_2$ towards HCOO$^-$. With the exception of polycrystalline Cu, this shift in FE is consistent with the general trend observed on various metals.[10] While the FE for HCOO$^-$ is highest at 2 °C (Fig. 5a), its rate of production (Fig. 5d) is highest at 22 °C. At 22 °C, the FE for HCOO$^-$ at Cu foams was 28(1)% at −1.3 V (Fig. 5a and
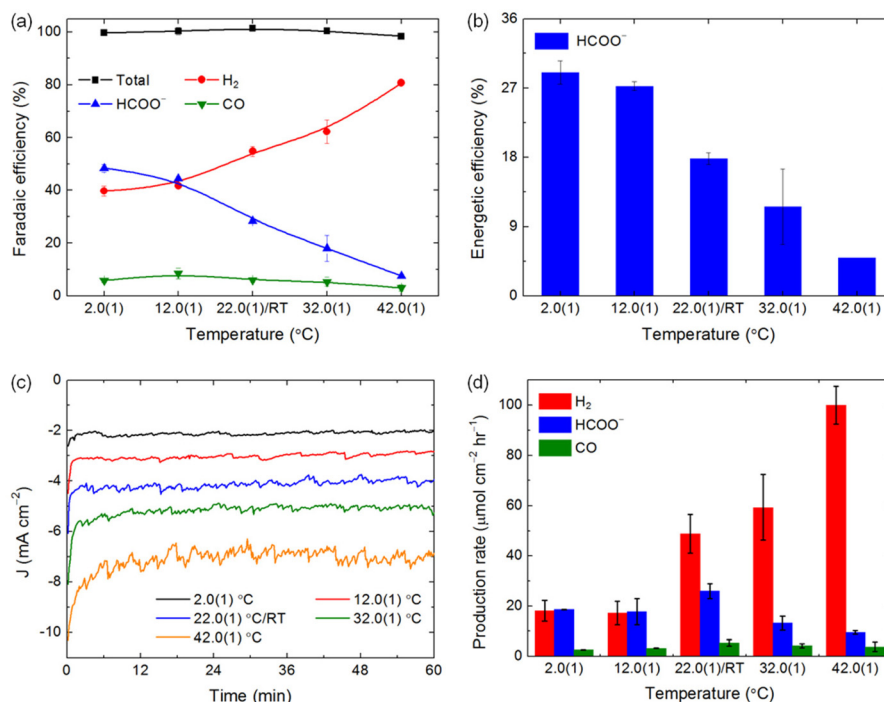

Fig. 5 Experimental data from electrocatalytic reduction of CO$_2$ at Cu foams at −1.30 V over a temperature range of 2.0(1) to 42.0(1) °C: (a) FE of major products, (b) EE of HCOO$^-$, (c) chronoamperograms *vs.* temperature, and (d) rates of production of major products.

Fig. S5c†) and 37(4)% at −1.2 V (Fig. S5c†). Other major products (*i.e.*, those produced at >5% FE) include CO and H_2. The amount of H_2 produced reflects the extent of the competing hydrogen evolution reaction (HER). This product distribution (*i.e.*, $HCOO^-$, CO, and H_2) was consistent across the temperature range studied. It is surprising that CH_4 and C_2H_4 are not produced at Cu foams at different temperatures (Table 2) given these compounds as well as $HCOO^-$, CO, and H_2 are produced as major products at Cu foils under a variety of reaction conditions.[9,10,25,49–51]

Small amounts (*i.e.*, <5% FE) of C_{2+} products such as ethane, ethanol, and propanol form at Cu foams (Table 2), which has been attributed to the retention of CO_2RR intermediates within the hierarchical porosity of the nanostructured electrocatalyst.[16,30] The absence of CH_4 product was surprising given the highly roughened surfaces of Cu foams. The formation of CH_4 is predicted to be more facile thermodynamically at a stepped Cu(211) facet, which is used to model stepped, kinked, and otherwise highly-roughened Cu surfaces.[40,52] Contrary to other studies using roughened or nanostructured Cu,[16,30,53] the surface of Cu foams is dominated by the Cu(111) facet, which preferentially produces $HCOO^-$ (*vide infra*). The different product distributions on Cu foams *vs.* Cu foils[54] indicates that not only electroactive area but also catalytic properties are altered by the nanostructured pores of the Cu foams.

Notably, the rate of production $HCOO^-$ on Cu foams competes with the rate of production of H_2 below RT. This observation is important because FE alone is an incomplete metric of an electrocatalyzed reaction. For example, the electrocatalytic reduction of CO_2 to CH_4 requires the transfer of eight electrons and protons. In contrast, the electrocatalytic conversion of protons from the electrolyte to H_2 requires the transfer of only two electrons. Consequently, H_2 is produced four times faster than CH_4 on a per molecule basis for the same FE. Therefore, the FE of CH_4 must be four times greater than the FE of H_2 for these two production rates to compete equivalently during electrocatalysis. The FE for CO remained <10% across the temperature range studied, which indicates <10% of the reaction follows the mechanistic pathway through adsorbed *COOH (the pathway that leads to CO).[52] This observation further supports that the formation of $HCOO^-$ at Cu foams predominantly follows the mechanistic pathway that passes through adsorbed HCOO*.

The onset potential for electrocatalysis shifts more negatively as the temperature is decreased (Fig. 6a). For example, the onset potential shifted from *ca.* −0.95 V at 42 °C to *ca.* −1.21 V at 2 °C when measured at a current density of −2 mA cm^{-2}. The potential at *ca.* −0.95 V more likely reflects the onset potential for the HER than the CO_2RR because at higher temperatures the HER dominates FE (Fig. 5a) and the concentration of CO_2 decreases in H_2O (*e.g.*, 73 mM at 2 °C *vs.* 21 mM at 42 °C).[55,56]

Table 2 Faradaic efficiencies for major and minor products from controlled potential electrolysis at −1.3 V (*vs.* Ag/AgCl) at Cu foam electrodes

Temp (°C)	pH	Faradaic efficiency (%)								
		Total	H_2	CO	CH_4	C_2H_4	C_2H_6	$HCOO^-$	C_2H_5OH	n-C_3H_7OH
2.0 ± 0.1	6.58(1)	99.73 ± 0.55	39.69 ± 1.87	5.85 ± 0.79	Trace[a]	0.57 ± 0.42	1.05 ± 0.52	48.36 ± 1.50	1.42 ± 0.07	0.73 ± 0.60
12.0 ± 0.1	6.61(1)	100.30 ± 1.42	41.61 ± 0.23	8.47 ± 2.06	Trace[a]	1.17 ± 0.08	1.31 ± 0.24	44.42 ± 0.51	0.49 ± 0.40	0.76 ± 0.62
22.0 ± 0.1	6.71(2)	101.37 ± 0.25	54.77 ± 1.92	5.95 ± 0.63	Trace[a]	3.06 ± 1.87	0.89 ± 0.73	28.41 ± 0.74	2.49 ± 0.14	1.59 ± 1.59
32.0 ± 0.1	6.82(2)	100.41 ± 0.52	62.25 ± 4.44	5.34 ± 1.68	Trace[a]	2.28 ± 0.66	5.56 ± 1.03	18.05 ± 4.89	2.38 ± 0.30	2.48 ± 0.49
42.0 ± 0.1	6.92(0)	98.39 ± 0.28	80.73 ± 0.64	3.01 ± 1.19	Trace[a]	0.50 ± 0.11	2.35 ± 0.47	7.53 ± 0.00	1.37 ± 0.18	0.62 ± 0.50

[a] "Trace" denotes products that were quantified but consistently accounted for <1% FE; values are omitted for clarity and to minimize over-interpreting minor products.
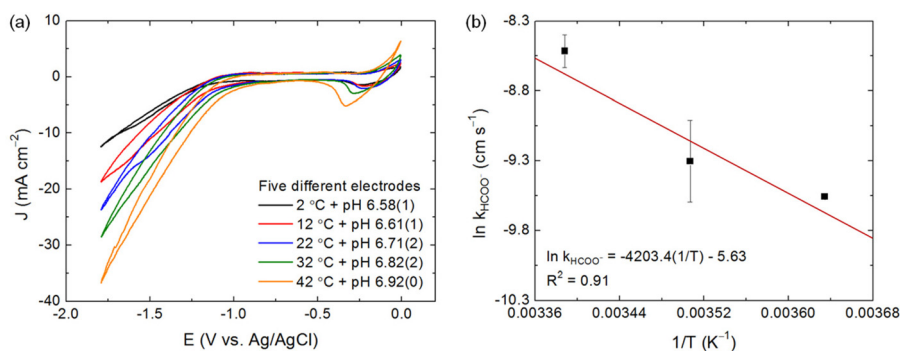

Fig. 6 (a) Cyclic voltammograms of five different Cu foam electrodes taken at different temperatures. Included in the legend are measured pH values that are used in the conversion of potential *vs.* Ag/AgCl to RHE and to calculate EE (*cf.*, Fig. 5b). Experimental conditions were: 0.1 M $KHCO_3$/H_2O electrolyte saturated with CO_2, 50 mV s^{-1} scan rate, *iR*-compensated. (b) Arrhenius plot of $\ln k_{HCOO^-}$ *vs.* 1/T for determining the activation energy for the formation of $HCOO^-$ at −1.3 V *vs.* Ag/AgCl at Cu foam electrodes.

The difference in concentration of CO_2 in H_2O and in 0.1 M $KHCO_3/H_2O$ is not trivial, notably that $[CO_2]$ in $KHCO_3/H_2O$ decreases with increasing bicarbonate salt concentration.[57] As expected, a parabolic trend in the rate of production of $HCOO^-$ (Fig. 5d) complicated a typical determination of temperature dependence. However, when considering only rates of production (*i.e.*, reaction rates) below 25 °C before the HER dominates,[58] the rate constants approximated the Arrhenius relationship (Fig. 6b). The activation energy for $HCOO^-$ at −1.3 V was 35 kJ mol^{-1} or 0.36 eV (compared to 50 kJ mol^{-1} or 0.52 eV for H_2). The formation of $HCOO^-$ at the Cu(111) facet *via* the HCOO* intermediate thermodynamically requires 0.33 eV.[40] The computational hydrogen electrode (CHE) model however, is purely thermodynamic and assumes kinetic barriers of uphill steps are minimal.[52,59] An experimental kinetic barrier is therefore expected to be greater than the computational thermodynamic requirement *via* the CHE model.

Conclusions

Developing electrochemical systems for use with carbon capture, utilization, and storage requires that the electrocatalysts deployed in these systems are highly selective, capable of being fabricated at scale, and low cost. The product distribution and product selectivity of the CO_2RR at nanostructured Cu foams differs from that obtained at polycrystalline Cu foils, notably significant FEs for $HCOO^-$ at low overpotential with little to no CH_4 or C_2H_4 produced. Grazing incidence X-ray diffraction was used to determine the dominant surface facet of Cu foams. Parameters for GIXRD experiments typically performed on non-porous, thin films were adapted to Cu foams to isolate its XRD pattern from that of the underlying Cu substrate. The dominant facet on the surface of Cu foams was determined to be Cu(111). Lower FEs for CO and a surface dominated by Cu(111) facets support the formation of $HCOO^-$ *via* the HCOO* intermediate at Cu foams.

The CO_2RR at Cu foams was studied over a range of temperatures (2 °C to 42 °C) chosen to reflect the operating temperatures for current and promising CO_2 capture media. Unlike that observed at polycrystalline Cu foils, the product distribution at Cu foams was consistently $HCOO^-$, CO, and H_2 at all temperatures. The rate constants to produce $HCOO^-$ at electrolyte temperatures below the standard temperature followed the Arrhenius relationship. The experimental activation energy was *ca.* 0.36 eV, which is consistent with a computational thermodynamic requirement of *ca.* 0.33 eV at Cu(111) facets *via* the HCOO* intermediate. While the FE for $HCOO^-$ approached 50% at 2 °C, the production rate, which includes both FE and current density, was highest at 22 °C.

Author contributions

S. T. A. and S. S. designed and performed the experiments. G. T. R. P. supervised the study and provided

Conflicts of interest

There are no conflicts to declare.

Acknowledgements

References

1 W. Ma, S. Xie, T. Liu, Q. Fan, J. Ye, F. Sun, Z. Jiang, Q. Zhang, J. Cheng and Y. Wang, *Nat. Catal.*, 2020, **3**, 478–487.

2 T. Zheng, K. Jiang and H. Wang, *Adv. Mater.*, 2018, **30**, 1802066.

3 E. I. Koytsoumpa, C. Bergins and E. Kakaras, *J. Supercrit. Fluids*, 2018, **132**, 3–16.

4 P. Gabrielli, M. Gazzani and M. Mazzotti, *Ind. Eng. Chem. Res.*, 2020, **59**, 7033–7045.

5 J. E. Huang, F. Li, A. Ozden, A. S. Rasouli, F. P. G. d. Arquer, S. Liu, S. Zhang, M. Luo, X. Wang, Y. Lum, Y. Xu, K. Bertens, R. K. Miao, C.-T. Dinh, D. Sinton and E. H. Sargent, *Science*, 2021, **372**, 1074–1078.

6 S. H. Lee and Y. Ahn, *J. Power Sources*, 2017, **351**, 67–73.

7 S. Ha, R. Larsen and R. I. Masel, *J. Power Sources*, 2005, **144**, 28–34.

8 X. Lu, D. Y. C. Leung, H. Z. Wang, M. K. H. Leung and J. Xuan, *ChemElectroChem*, 2014, **1**, 836–849.

9 Y. Hori, H. Wakebe, T. Tsukamoto and O. Koga, *Electrochim. Acta*, 1994, **39**, 1833–1839.

10 M. Azuma, K. Hashimoto, M. Hiramoto, M. Watanabe and T. Sakata, *J. Electrochem. Soc.*, 1990, **137**, 1772–1778.

11 Y. Hori, K. Kikuchi, A. Murata and S. Suzuki, *Chem. Lett.*, 1986, 897–898.

12 S. T. Ahn, I. Abu-Baker and G. T. R. Palmore, *Catal. Today*, 2017, **288**, 24–29.

13 W. Tang, A. A. Peterson, A. S. Varela, Z. P. Jovanov, L. Bech, W. J. Durand, S. Dahl, J. K. Nørskov and I. Chorkendorff, *Phys. Chem. Chem. Phys.*, 2012, **14**, 76–81.

14 L. Ou and Z. He, *ACS Omega*, 2020, **5**, 12735–12744.

15 P. D. Luna, R. Quintero-Bermudez, C.-T. Dinh, M. B. Ross, O. S. Bushuyev, P. Todorović, T. Regier, S. O. Kelley, P. Yang and E. H. Sargent, *Nat. Catal.*, 2018, **1**, 103–110.

16   S. Sen, D. Liu and G. T. R. Palmore, *ACS Catal.*, 2014, **4**, 3091–3095.

17   T. Kim and G. T. R. Palmore, *Nat. Commun.*, 2020, **11**, 3622.

18   C. S. Chen, A. D. Handoko, J. H. Wan, L. Ma, D. Ren and B. S. Yeo, *Catal. Sci. Technol.*, 2015, **5**, 161–168.

19   O. A. Baturina, Q. Lu, M. A. Padilla, L. Xin, W. Z. Li, A. Serov, K. Artyushkova, P. Atanassov, F. Xu, A. Epshteyn, T. Brintlinger, M. Schuette and G. E. Collins, *ACS Catal.*, 2014, **4**, 3682–3695.

20   H. C. Shin, J. Dong and M. L. Liu, *Adv. Mater.*, 2003, **15**, 1610–1614.

21   S. H. Smallcombe, S. L. Patt and P. A. Keifer, *J. Magn. Reson., Ser. A*, 1995, **117**, 295–303.

22   *CRC Handbook of Chemistry and Physics*, ed. W. M. Haynes, D. R. Lide and T. J. Bruno, CRC Press, Boca Raton, FL, 2016.

23   M. Gattrell, N. Gupta and A. Co, *J. Electroanal. Chem.*, 2006, **594**, 1–19.

24   R. C. Dorf, *The Electrical Engineering Handbook: Electronics, Power Electronics, Optoelectronics, Microwaves, Electromagnetics, and Radar*, CRC/Taylor & Francis, Boca Raton, FL, 3rd edn, 2006.

25   K. P. Kuhl, E. R. Cave, D. N. Abram and T. F. Jaramillo, *Energy Environ. Sci.*, 2012, **5**, 7050–7059.

26   A. J. Bard and L. R. Faulkner, *Electrochemical Methods: Fundamentals and Applications*, Wiley, New York, 2nd edn, 2001.

27   S. Ponnurangam, C. M. Yun and I. V. Chernyshova, *ChemElectroChem*, 2016, **3**, 74–82.

28   J. F. Xie, Y. X. Huang, W. W. Li, X. N. Song, L. Xiong and H. Q. Yu, *Electrochim. Acta*, 2014, **139**, 137–144.

29   C. W. Li and M. W. Kanan, *J. Am. Chem. Soc.*, 2012, **134**, 7231–7234.

30   A. Dutta, M. Rahaman, N. C. Luedi and P. Broekmann, *ACS Catal.*, 2016, **6**, 3804–3814.

31   F. S. Roberts, K. P. Kuhl and A. Nilsson, *Angew. Chem., Int. Ed.*, 2015, **54**, 5179–5182.

32   M. Nauer, K. Ernst, W. Kautek and M. Neumann-Spallart, *Thin Solid Films*, 2005, **489**, 86–93.

33   P. Colombi, P. Zanola, E. Bontempi and L. E. Depero, *Spectrochim. Acta, Part B*, 2007, **62**, 554–557.

34   D. Simeone, G. Baldinozzi, D. Gosset, S. Le Caer and J. F. Berar, *Thin Solid Films*, 2013, **530**, 9–13.

35   Y. Hori, H. Wakebe, T. Tsukamoto and O. Koga, *Electrochim. Acta*, 1994, **39**, 1833–1839.

36   Y. Hori, in *Modern Aspects of Electrochemistry*, ed. C. G. Vayenas, R. E. White and M. E. Gamboa-Aldeco, Springer, New York, NY, 2008, vol. 42.

37   Y. Hori, K. Kikuchi and S. Suzuki, *Chem. Lett.*, 1985, **14**, 1695–1698.

38   Y. Hori, I. Takahashi, O. Koga and N. Hoshi, *J. Phys. Chem. B*, 2002, **106**, 15–17.

39   J. S. Yoo, R. Christensen, T. Vegge, J. K. Norskov and F. Studt, *ChemSusChem*, 2016, **9**, 358–363.

40   W. J. Durand, A. A. Peterson, F. Studt, F. Abild-Pedersen and J. K. Nørskov, *Surf. Sci.*, 2011, **605**, 1354–1359.

41   A. Verdaguer-Casadevall, C. W. Li, T. P. Johansson, S. B. Scott, J. T. McKeown, M. Kumar, I. E. L. Stephens, M. W. Kanan and I. Chorkendorff, *J. Am. Chem. Soc.*, 2015, **137**, 9808–9811.

42   X. F. Feng, K. L. Jiang, S. S. Fan and M. W. Kanan, *J. Am. Chem. Soc.*, 2015, **137**, 4606–4609.

43   C. T. Chantler, *J. Phys. Chem. Ref. Data*, 1995, **24**, 71–591.

44   C. T. Chantler, *J. Phys. Chem. Ref. Data*, 2000, **29**, 597–1048.

45   S. P. Kang and H. Lee, *Environ. Sci. Technol.*, 2000, **34**, 4397–4400.

46   D. DeCiccio, S. T. Ahn, S. Sen, F. Schunk, G. T. R. Palmore and C. Rose-Petruck, *Electrochem. Commun.*, 2015, **52**, 13–16.

47   U. E. Aronu, S. Gondal, E. T. Hessen, T. Haug-Warberg, A. Hartono, K. A. Hoff and H. F. Svendsen, *Chem. Eng. Sci.*, 2011, **66**, 6393–6406.

48   D. L. Tong, J. P. M. Trusler, G. C. Maitland, J. Gibbins and P. S. Fennell, *Int. J. Greenhouse Gas Control*, 2012, **6**, 37–47.

49   Y. Hori, A. Murata and R. Takahashi, *J. Chem. Soc., Faraday Trans. 1*, 1989, **85**, 2309–2326.

50   R. Reske, H. Mistry, F. Behafarid, B. R. Cuenya and P. Strasser, *J. Am. Chem. Soc.*, 2014, **136**, 6978–6986.

51   A. S. Varela, M. Kroschel, T. Reier and P. Strasser, *Catal. Today*, 2016, **260**, 8–13.

52   A. A. Peterson, F. Abild-Pedersen, F. Studt, J. Rossmeisl and J. K. Nørskov, *Energy Environ. Sci.*, 2010, **3**, 1311–1315.

53   A. Loiudice, P. Lobaccaro, E. A. Kamali, T. Thao, B. H. Huang, J. W. Ager and R. Buonsanti, *Angew. Chem., Int. Ed.*, 2016, **55**, 5789–5792.

54   K. Jiang, R. B. Sandberg, A. J. Akey, X. Liu, D. C. Bell, J. K. Nørskov, K. Chan and H. Wang, *Nat. Catal.*, 2018, **1**, 111–119.

55   R. Crovetto, *J. Phys. Chem. Ref. Data*, 1991, **20**, 575–589.

56   J. J. Carroll, J. D. Slupsky and A. E. Mather, *J. Phys. Chem. Ref. Data*, 1991, **20**, 1201–1209.

57   C. S. Wong, P. Y. Tishchenko and W. K. Johnson, *J. Chem. Eng. Data*, 2005, **50**, 817–821.

58   M. Liu, Y. J. Pang, B. Zhang, P. De Luna, O. Voznyy, J. X. Xu, X. L. Zheng, C. T. Dinh, F. J. Fan, C. H. Cao, F. P. G. de Arquer, T. S. Safaei, A. Mepham, A. Klinkova, E. Kumacheva, T. Filleter, D. Sinton, S. O. Kelley and E. H. Sargent, *Nature*, 2016, **537**, 382–386.

59   F. Calle-Vallejo and M. T. M. Koper, *Angew. Chem., Int. Ed.*, 2013, **52**, 7282–7285.